

Practical H₂ supply from ammonia borane enabled by amorphous iron domain

Received: 6 December 2023

Accepted: 16 October 2024

Published online: 23 October 2024

Check for updates

Yufeng Chen^{1,6}, Zhongling Lang^{2,6}, Kun Feng¹, Kang Wang¹, Yangguang Li², Zhenhui Kang¹, Lin Guo³✉, Jun Zhong¹✉ & Jun Lu^{4,5}✉

Efficient catalysis of ammonia borane (AB) holds potential for realizing controlled energy release from hydrogen fuel and addressing cost challenges faced by hydrogen storage. Here, we report that amorphous domains on metallic Fe crystal structures (R-Fe₂O₃ Foam) can achieve AB catalytic performances and stability (turnover frequency (TOF) of 113.6 min⁻¹, about 771 L H₂ in 900 h, and 43.27 mL/(min·cm²) for 10×10 cm² of Foam) that outperform reported benchmarks (most <14 L H₂ in 45 h) by at least 20 times. These notable increases are enabled by the stable Fe crystal structure, while defects and unsaturated atoms in the amorphous domains form Fe-B intermediates that significantly lower the dissociation barriers of H₂O and AB. Given that the catalyst lifetime is a key determinant for the practical use in fuel cells, our R-Fe₂O₃ Foam also provides decent H₂ supply (180 mL H₂/min, AB water solution of 7.5 wt% H₂) in a driven commercial car fuel cell at stable power outputs (7.8 V and 1.6 A for at least 5 h). When considered with its facile synthesis method, these materials are potentially very promising for realizing durable high-performance AB catalysts and viable chemical storage in hydrogen powered vehicles.

Hydrogen energy is attractive as a fuel source since it can enable zero greenhouse gas emissions and a sustainable economy^{1–3}. Hydrogen can also be produced in a clean way^{4,5}. Although hydrogen-based technologies have been researched since the 1970s, hydrogen storage and release remain costly and impractical for commercial use in vehicles^{3,6–9}. Storing H₂ gas in compression has been a common approach, but may raise safety risks for drivers, prompting the development of alternative methods such as chemical storage¹⁰. Here, catalysts facilitate the release of H₂ gas from chemicals when combined with H₂O solution, and ammonia borane (AB) is notable for its high hydrogen content (19.6 wt%), high stability in air and water, and non-toxicity^{6–11}. Under the action of suitable catalysts, 1 mol AB water solution can be hydrolyzed at room temperature to release 3 mol H₂.

The stable and non-toxic nature of solid AB enables it to be well stored and transported, resulting in a high gravimetric hydrogen storage capacity (GHSC) when compared to similar chemicals such as NaBH₄ or LiBH₄ (highly flammable and toxic). Despite obvious advantages over the storage of compressed H₂ (detailed in Supplementary Figs. 1 and 2), catalysts for AB hydrolysis cannot yet achieve necessary performances, and stability in particular is a challenge that prevents practical catalyst lifetimes (normally <2 h; benchmark 45 h was achieved with Rh but its activity sharply decreased in 9 h)^{6–19}.

Methods to precisely engineer micro or nanostructures can enable high catalytic activity, as has been reported, but these come at the cost of stability in harsh reaction environments. Bulk materials, on the other hand, are stable but less catalytically active. Synthesis of fine

¹Institute of Functional Nano and Soft Materials Laboratory (FUNSOM), Jiangsu Key Laboratory for Carbon-Based Functional Materials & Devices, Soochow University, Suzhou, China. ²Key Laboratory of Polyoxometalate and Reticular Material Chemistry of Ministry of Education, Faculty of Chemistry, Northeast Normal University, Changchun, China. ³School of Chemistry, Beijing Advanced Innovation Center for Biomedical Engineering, Key Laboratory of Bio-Inspired Smart Interfacial Science and Technology, Beihang University, Beijing, China. ⁴College of Chemical and Biological Engineering, Zhejiang University, Hangzhou, China. ⁵Quzhou Institute of Power Battery and Grid Energy Storage, Quzhou, China. ⁶These authors contributed equally: Yufeng Chen, Zhongling Lang. ✉e-mail: guolin@buaa.edu.cn; jzhong@suda.edu.cn; junzoelu@zju.edu.cn

nano/microstructures onto bulk materials has also been reported to enhance mechanical properties but not improve bulk catalytic activity²⁰. Recent reports of amorphous domains in nanomaterials have achieved notable catalytic activity due to abundant active sites^{21,22}. The internal amorphous defects could even transform the non-active material into a highly active catalyst²³. Thus the successful creation of amorphous domains in the whole crystal structures extending from nanomaterials to bulk materials may enable a combinatorial approach to catalyst design for performance and stability²⁴.

The abundance, low-cost, and easily manipulated crystal structure of Iron (Fe) make it a suitable material for AB hydrolysis if catalytic activity can be improved. Although some Fe-based nanomaterials might have certain activity¹¹, bulk Fe metal (a block of metallic Fe) has never been reported for efficient AB hydrolysis. However, with a facile oxidation and reduction process, here we report the synthesis of amorphous domains in metallic Fe Foam (R-Fe₂O₃) that achieve notable performances (TOF of 113.6 min⁻¹, about 771 L H₂ in 900 h, and 43.27 mL/(min·cm²) for 10 × 10 cm² of Foam) for AB hydrolysis. These amorphous domains contain defects and unsaturated atoms, which form Fe-B intermediates during hydrolysis, thereby lowering dissociation barriers of H₂O and AB (according to theoretical calculations), while the bulk Fe crystal structure maintains catalyst stability.

Amorphous domains have been verified through transmission electron microscopy (TEM) and synchrotron radiation X-ray absorption spectroscopy (XAS). The combined benefits of these domains in bulk materials enable the remarkable increase in catalyst lifetime and have even provided onboard H₂ supply (180 mL/min) in a commercial car fuel cell for at least 5 h (at the power output of 7.8 V and 1.6 A). By storing AB as a solid and adding water in stoichiometric amounts, this system achieves a high GHSC of 7.5 wt% H₂ from AB, which meets the U.S. Department of Energy (DOE) target¹⁹. Therefore, this facile approach to creating amorphous domains onto bulk materials, especially metallic Fe, holds promise for enabling the use of AB chemical storage in hydrogen-powered vehicles.

Results and discussion

Efficient and stable hydrolysis of ammonia-borane

Commercial Fe Foam is almost inactive, and no hydrogen (H₂) can be released from AB even after 1 h, as shown in Fig. 1a. Commercial Fe₂O₃ nanoparticles (NPs) are also inactive in 1 h. The Fe Foam was activated by simple oxidation in air and a following reduction directly in the AB solution. Interestingly, the modified Fe Foam can be effectively used for the hydrolysis of AB, as shown in Fig. 1a. The sample after oxidation is labeled as Fe₂O₃ Foam (800 °C) and the reduced sample is labeled as

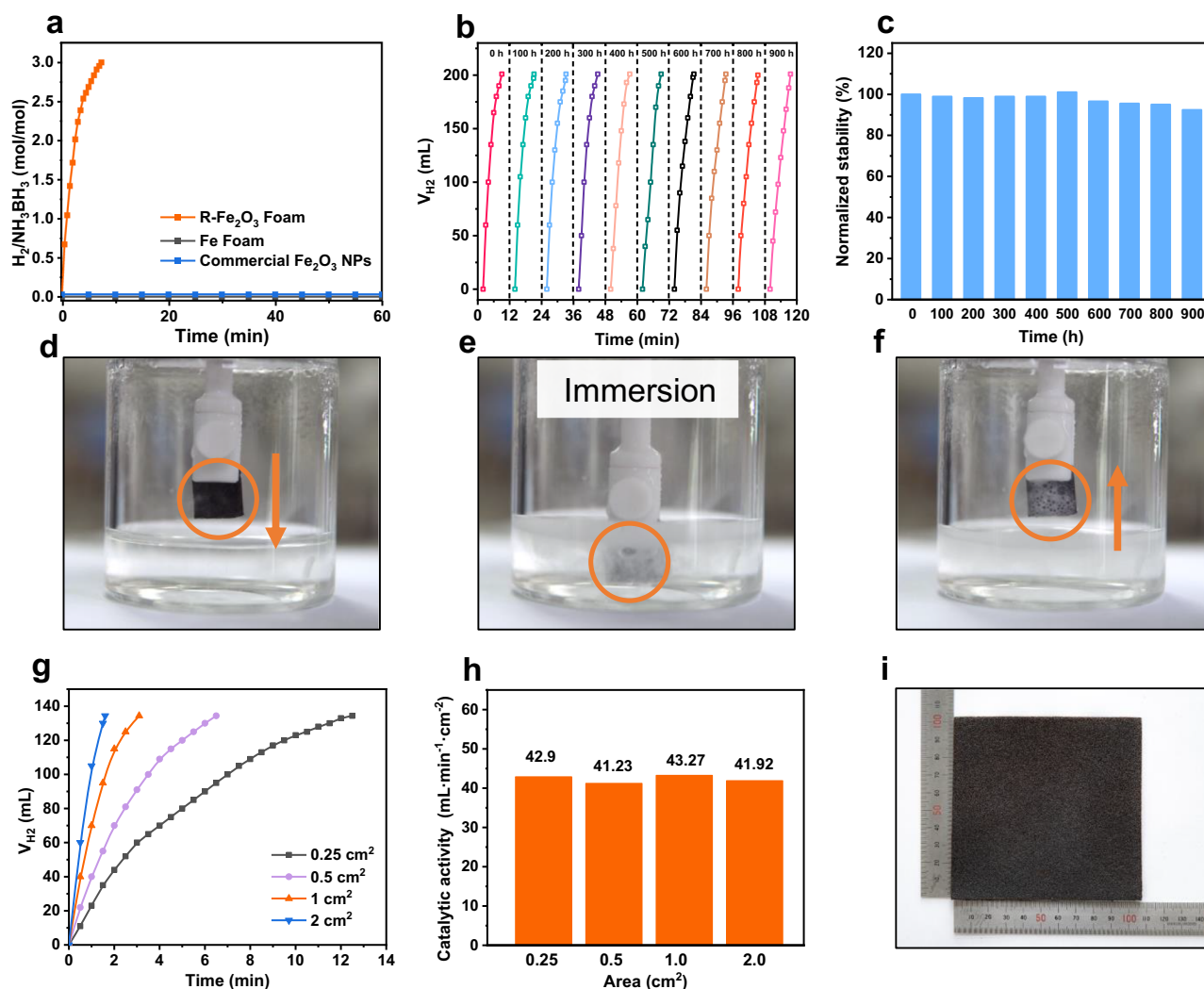


Fig. 1 | The catalytic performance of R-Fe₂O₃ Foam (800 °C) in the hydrolysis of AB aqueous solution. a Hydrogen evolution curves of the hydrolysis of AB catalyzed by Fe Foam, commercial Fe₂O₃ NPs, and R-Fe₂O₃ Foam (800 °C), respectively. **b, c** Stability test of R-Fe₂O₃ Foam (800 °C) within 900 h. After 900 h, there is no

obvious decline. **d–f** Hydrolysis process of AB catalyzed by R-Fe₂O₃ Foam (800 °C). **g** Hydrogen evolution curves catalyzed by R-Fe₂O₃ Foam (800 °C) with different sizes. **h** Area activities of R-Fe₂O₃ Foam (800 °C) with different sizes. **i** Picture of R-Fe₂O₃ Foam (800 °C) with a size of 10 × 10 cm².

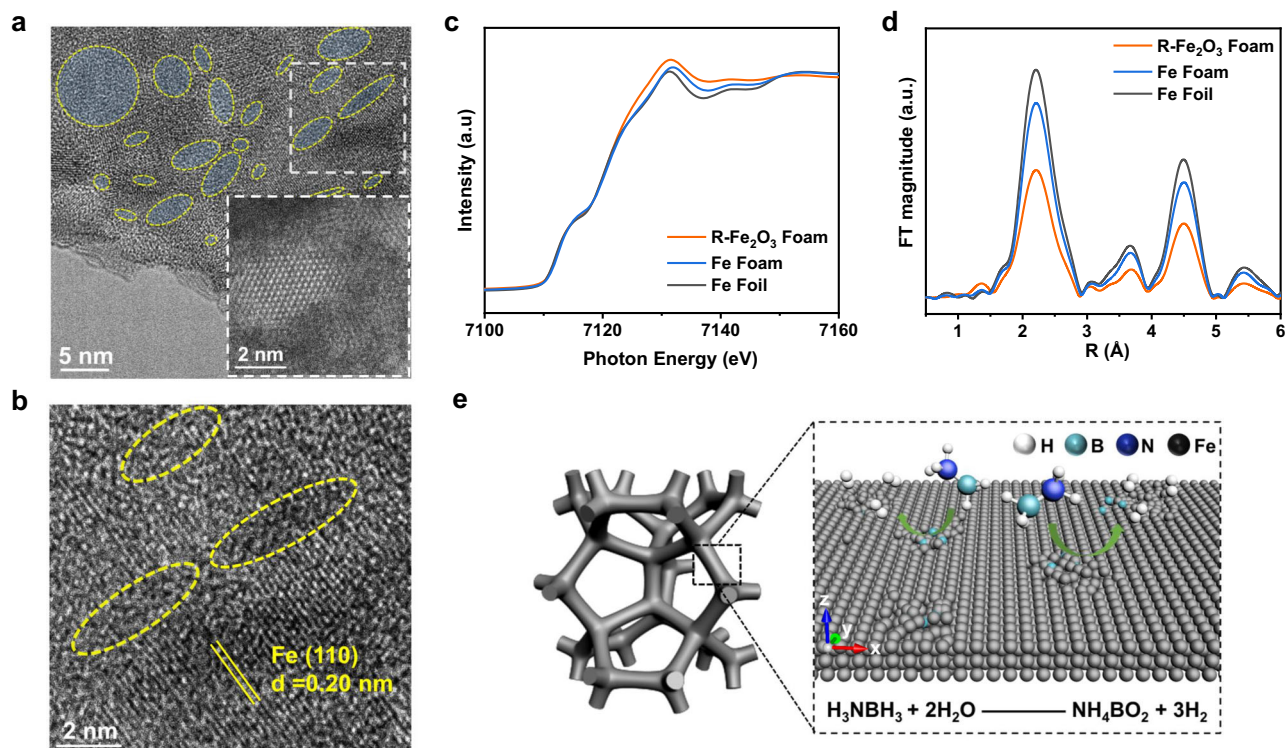


Fig. 2 | The structure information of R-Fe₂O₃ Foam (800 °C). **a, b** TEM and HRTEM images of R-Fe₂O₃ Foam (800 °C), respectively. The inset in Fig. 2a shows the aberration-corrected HAADF-STEM image. **c, d** Fe K-edge XANES spectra and

Fourier transform curves of the EXAFS data of R-Fe₂O₃ Foam (800 °C) and some reference samples, respectively. **e** Illustration of the hydrolysis of AB on R-Fe₂O₃ Foam (800 °C).

R-Fe₂O₃ Foam (800 °C). The experimental illustration is shown in Supplementary Fig. 3a, and the details can be found in Methods.

The catalytic performance of R-Fe₂O₃ Foam (800 °C) ($1 \times 1 \text{ cm}^2$) in the hydrolysis of AB aqueous solution is shown in Fig. 1a, which can fully produce 201 mL H₂ (3 mol H₂ produced from 1 mol AB) in 7.5 min. The volume of H₂ generation was measured by recording the displacement of water and the produced gas was identified using a gas chromatograph. Figure 1d–f show the images when the R-Fe₂O₃ Foam is immersed in AB solution and then removed. It should be noted that R-Fe₂O₃ Foam (800 °C) can be directly used as a catalyst without any substrate. The AB solution is very stable at room temperature. However, with the immersion of panel-like R-Fe₂O₃ Foam, large amounts of H₂ bubbles can be observed, and the reaction can be quickly stopped when the Foam is removed. Details can be found in Supplementary Movie 1. The calculated area activity of R-Fe₂O₃ Foam (800 °C) is a high value of 43.27 mL H₂/(min·cm²) (using the process to release 134 mL H₂ since the left 1/3 process is slow; for the full process, the activity is 26.90 mL H₂/(min·cm²)). The calculated TOF value is 113.6 (H₂) mol/(Cat-Fe) mol·min (using the process to release 134 mL H₂ and the surface Fe as active sites, details can be found in the Methods part), which is also a notable high value compared to the benchmark non-noble metal catalysts (Supplementary Table 1)^{14,15}.

Critically, the R-Fe₂O₃ Foam (800 °C) catalyst shows remarkable long-term stability along with high efficiency. The hydrolysis was continuously catalyzed by R-Fe₂O₃ Foam (800 °C) in AB solution for 900 h without obvious decline, which far exceeded catalysts reported in the literature that was only stable for a few hours or several cycles (Supplementary Table 1). The Foam was taken out to carefully measure its catalytic activity every 5 h. The Foam does not require washing or other treatment and large amounts of H₂ can be continuously observed in the whole process. As shown in Fig. 1b, c (also see Supplementary Fig. 4a, b), there is no obvious activity decline even after operating for 900 h (keep more than 92% of the initial activity), which

sets the benchmark for all catalysts ever used for the hydrolysis of AB (both noble and non-noble metal catalysts). Supplementary Fig. 4c also shows the hydrolysis curves before and after use for 500 h, with no obvious difference between the two curves. To highlight the excellent stability of our sample, we show a performance comparison to many others reported in the literature in Supplementary Table 1. It is clear that the catalysts in literature can only last for a few hours or several cycles (most less than 2 h; the benchmark Rh₀/Co₃O₄ showed a total 45 h lifetime, but its activity sharply decreased in 9 h), while the presented R-Fe₂O₃ Foam (800 °C) far exceeds this standard by continuously producing large H₂ amounts for at least 900 h. The catalyst can totally work for 1100 h until 20% of the initial activity. The used catalyst also shows excellent reusability, which can work for another 300 h after the same oxidation-reduction treatment.

Structure information of R-Fe₂O₃ foam

Detailed structure information of R-Fe₂O₃ Foam (800 °C) has been investigated to understand the unprecedented performance. Supplementary Fig. 3b–d shows a comparison of the scanning electron microscopy (SEM) images for Fe Foam, Fe₂O₃ Foam (800 °C), and R-Fe₂O₃ Foam (800 °C), respectively, where there is no significant difference except for some cracks observed in R-Fe₂O₃ Foam (800 °C). Figure 2a, b shows the TEM and HRTEM images of R-Fe₂O₃ Foam (800 °C), respectively. Metallic Fe (110) lattice in R-Fe₂O₃ Foam (800 °C) can be observed in Fig. 2b, which is similar to the pristine Fe Foam (Supplementary Fig. 5a, e, confirmed by XRD data in Supplementary Fig. 6a). However, clear amorphous Fe domains (labeled by ellipses) can be observed in Fig. 2b, which is significantly different from the perfect crystal structure of Fe Foam in Supplementary Figs. 5a, e. The amorphous domains can be easily observed in R-Fe₂O₃ Foam (800 °C) shown in Fig. 2a (the ellipses), suggesting that large distributions of amorphous Fe domains can be found in the as-produced sample. For comparison, the original Fe Foam shows perfect Fe crystal structure

(Supplementary Fig. 5a). The inset of Fig. 2a also shows the aberration-corrected high angle annular dark field scanning transmission electron microscopy (HAADF-STEM) image of R-Fe₂O₃ Foam (800 °C), confirming the existence of amorphous domains.

To further verify the existence of abundant amorphous Fe domains in R-Fe₂O₃ Foam (800 °C), XAS spectra at Fe K-edge are measured and shown in Fig. 2c, d. Figure 2c shows the X-ray Absorption Near Edge Structure (XANES) spectrum of R-Fe₂O₃ Foam (800 °C) that is very similar to that of pure Fe foil and Fe Foam, confirming the main metallic content is Fe. However, compared to the pristine Fe Foam and Fe foil, the Extended X-ray Absorption Fine Structure (EXAFS) features of R-Fe₂O₃ Foam (800 °C) in Fig. 2d show much lower peak intensities, suggesting more vacancies or unsaturated atoms due to the existence of amorphous domains²⁵. We also show the fitting results of EXAFS data in Supplementary Table 2, where the R-Fe₂O₃ Foam exhibits a significantly reduced Fe coordination number, strongly confirming the existence of amorphous domains with defects and vacancies, as illustrated in Fig. 2e.

Practical H₂ supply from hydrolysis of AB

R-Fe₂O₃ Foam with the aforementioned amorphous domains showed excellent catalytic performance and ultra-high stability that is suitable for fuel cells used in practical H₂ supply. When used in a commercial fuel cell, the H₂ production system (AB solution and R-Fe₂O₃ Foam) even powered a model car. As shown in Supplementary Movie 2 and Movie 3, the Foam can be used to produce a high H₂ flow (180 mL H₂/min) in the commercial fuel cell, which can successfully power the driven model car for long durations (total of at least 5 h). A stable output of 7.8 V and 1.6 A is obtained (12 W), which is usable as a power supply for various applications. As shown in Supplementary Movie 3, the onboard system (with a practical AB concentration of 19.0 wt%) can independently drive the model car for a long time. The system on the model car only contains the fuel cell, the water for filtration, and the reaction cell with AB, water, and catalyst. The water for filtration (5 g pure water) has been used to remove small amounts of evaporated NH₃ and water due to the exothermic process (only 12 ppm NH₃ left in H₂ after filtration). The panel-like Foam can also be easily removed to control the reaction, this is favorable for real applications where the device can be easily powered off.

Beneficially, the reaction can be enlarged by using larger sizes of panel-like foam. In Fig. 1g, h, the catalytic performances of R-Fe₂O₃ Foam (800 °C) samples with different sizes have been shown to exhibit similar area activities. The produced H₂ can thus be linearly increased with Foam size. At present, a Foam size of 10 × 10 cm² (Fig. 1i) can be easily prepared to produce more than 4000 mL H₂ per minute. The H₂ production rate can also be further accelerated by combining several Foams to form an array to produce large amounts of H₂ to meet the requirement for high energy density devices.

Gravimetric hydrogen storage capacity (GHSC) is a factor and the DOE ultimate target for on-board H₂ storage is 7.5 wt% H₂¹⁹. The GHSC of AB aqueous solution is around 5.0 wt% H₂²⁶. AB is in powder form and very stable in air, thus making it suitable as a fuel. By storing AB as a solid and adding water in stoichiometric amounts¹⁸, the GHSC of AB water solution using the Foam can achieve a suitably high value of 8.91 wt% H₂ (see Supplementary Table 3), exceeding the DOE target. Recycle water from fuel cells can be used, as shown in Supplementary Fig. 3b. For a practical process, the GHSC value can also achieve 7.5 wt% H₂ by storing AB as a solid and using the recycled water (with an AB concentration around 19.0 wt%), as illustrated in Supplementary Movie 2 (step by step) and Supplementary Fig. 7. Thus, the controlled release of H₂ from AB can be realized with the low-cost and abundant Fe catalyst. For clarity, the mass, overall outer volume, porosity, and specific surface area of the catalyst are listed in Supplementary Table 4. The concentration, weight, volume, GHSC, and specific system energy

density of AB solution are also shown in Supplementary Table 5. The onboard system can achieve a high specific system energy density of 2.50 kWh/kg (or 2.26 kWh/L). For comparison, H₂ in a tank only shows a volumetric energy density of 0.8 kWh/L for H₂ at 350 bar and 1.3 kWh/L at 700 bar, respectively. The presented onboard system can also drive a drone, as shown in Supplementary Movie 4. Along with the decreased cost of producing AB at global scales and the efficient regeneration of spent fuel, catalysts that realize the use of AB may build a clean, safe, and renewable hydrogen energy system in the near future.

Catalytic details are shown in Supplementary Fig. 8. Temperature dependence curves of R-Fe₂O₃ Foam (800 °C) are shown in Supplementary Fig. 8a, where catalytic activity increases with temperature. Supplementary Fig. 8b shows the Arrhenius plot, revealing a low activation energy of 20.74 kJ/mol. The AB concentration dependence curves with the same R-Fe₂O₃ Foam are shown in Supplementary Fig. 8c, revealing a weak relationship between the reaction rate and the AB concentration. Supplementary Fig. 8d shows the logarithmic plots of the reaction rate versus the AB concentration, which follows zero-order kinetics.

The facile oxidation and reduction method can be used to prepare various metallic Foams for the hydrolysis of AB, as shown in Supplementary Fig. 9. R-CuO Foam and R-NiO Foam show much lower catalytic performance than that of R-Fe₂O₃ Foam. R-CoO Foam shows a high catalytic activity similar to that of R-Fe₂O₃ Foam. Unfortunately, the lifetime stability of R-CoO Foam is unacceptable as a sharp decrease (50% left) occurs after 10 h of operation, as shown in Supplementary Fig. 4d. Thus, R-Fe₂O₃ Foam (800 °C) remains the best choice for the hydrolysis of AB in all these metals.

In situ XAS experiments and working mechanism

The catalytic mechanism of R-Fe₂O₃ Foam (800 °C) with amorphous domains has been further investigated. Initially, the oxidation effect has been studied, and catalytic curves of the samples sintered at different temperatures (reduced by the same AB solution) are shown in Fig. 3a. The sample sintered at a low temperature of 300 °C provides unsatisfied operation, while all the samples sintered at temperatures above 500 °C show excellent performance. XRD spectra in Supplementary Fig. 6b reveal that the sample sintered at 300 °C (without further reduction) preserves a metallic structure, while samples sintered at temperatures above 500 °C are mostly oxidized. Supplementary Fig. 5b, f also shows the TEM images of Fe₂O₃ Foam (800 °C) (before AB reduction), exhibiting perfect Fe₂O₃ crystal structure and confirming that active amorphous domains have been created in the AB reduction process. Complete oxidation at high temperatures can lead to reduction changes, which can form amorphous domains in the bulk to favor the hydrolysis reaction.

The reduction process has also been carefully probed and compared by using different reduction agents such as NaBH₄ or LiBH₄ solutions, H₂ gas, and N₂H₄ solution (detailed treatments can be found in the “Methods”). All the above reduction agents are highly reductive, and some of them have been processed at high temperatures (H₂) or using the refluxing process (N₂H₄) (for AB, it is only immersed in the solution for 20 min). Corresponding catalytic curves are shown in Fig. 3b. The reductive N₂H₄ solution with similar elements of N and H as that in AB was used to reduce the Fe₂O₃ Foam (800 °C) but with inferior catalytic performance. According to the XRD data in Supplementary Fig. 6c, the N₂H₄-treated sample is still oxidized, similar to Fe₂O₃ Foam (800 °C), suggesting that N₂H₄ hardly reduces the bulk composition of Fe₂O₃ Foam (800 °C) even with refluxing. However, by using B-based agents such as NaBH₄ or LiBH₄ solutions, the Fe₂O₃ Foam can be successfully reduced according to XRD data (Supplementary Fig. 6c). Moreover, the catalytic performances for both NaBH₄ and LiBH₄ treated samples are also noteworthy, suggesting that B has an important role in both the reduction and the catalytic processes. B-based reduction agents can effectively react with Fe₂O₃ to produce

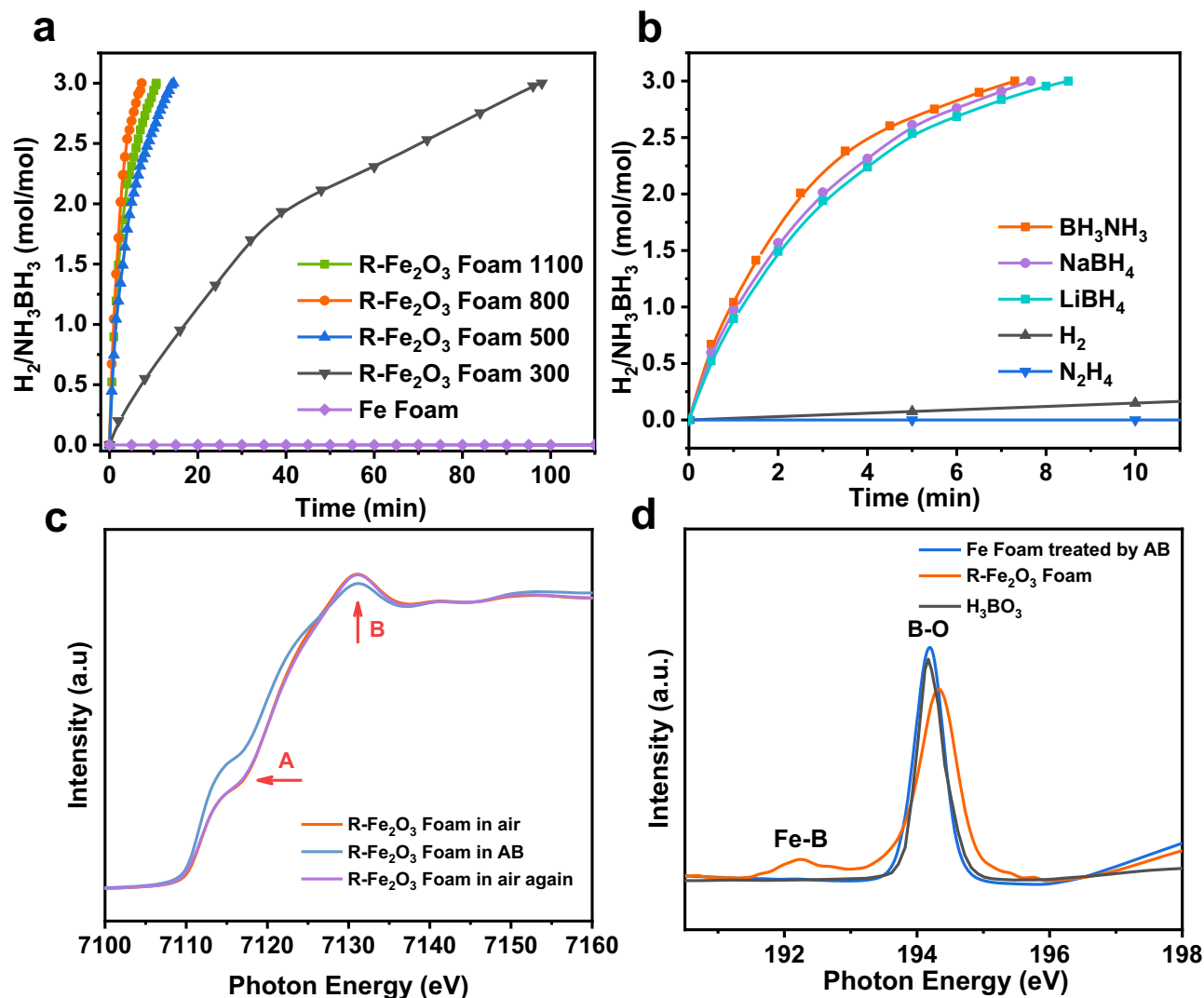


Fig. 3 | Working mechanism of R-Fe₂O₃ Foam (800 °C) for the efficient and stable hydrolysis of AB. **a** Hydrogen evolution curves catalyzed by Fe Foam and R-Fe₂O₃ Foam samples sintered at different temperatures (300, 500, 800, and 1100 °C). **b** Hydrogen evolution curves catalyzed by R-Fe₂O₃ Foam (800 °C) samples

reduced by different agents. **c** In situ XANES spectra of R-Fe₂O₃ Foam (800 °C) in air and immersed in AB at Fe K-edge. **d** B K-edge XANES spectra of R-Fe₂O₃ Foam (800 °C), Fe Foam treated by AB and the H₃BO₃ reference.

metallic Fe and create amorphous Fe domains to enhance the catalytic performance. Consequently, R-Fe₂O₃ Foam (800 °C) is an efficient and stable catalyst for the hydrolysis of both NaBH₄ and LiBH₄ to release H₂. It should be noted that XRD data have an analysis depth of many tens of micrometers, and the Foam branches are around 100 μm thick. When the fully oxidized Fe₂O₃ Foam (800 °C) was treated with acid to remove the outside oxidation layer, the inner part was found to be metallic Fe which could maintain the skeleton structure. The oxidized Foam is initially inactive to the hydrolysis, until reduced in AB solution for 20 min to create amorphous Fe domains. The highly active R-Fe₂O₃ Foam (800 °C) will lose its activity when heated in air at 60 °C with more oxidized parts, suggesting that the oxidized parts are not active sites for hydrolysis.

To confirm the critical role of amorphous domains, the Fe₂O₃ Foam (800 °C) has also been reduced by H₂ at high temperatures (1100 °C). XRD data in Supplementary Fig. 6c clearly indicate that the H₂-treated Foam has been successfully reduced. However, the catalytic performance of the H₂-treated R-Fe₂O₃ Foam (800 °C) is ordinary in Fig. 3b and can be attributed to high-temperature treatment in the H₂-based reduction, which can remove defects and construct a fine crystal structure. As a result, the TEM images of H₂-treated R-Fe₂O₃ Foam

(800 °C) in Supplementary Fig. 5c, g show a superior metallic Fe crystal structure without amorphous domains. Thus, the active sites have been removed and the H₂-treated sample shows unsatisfied catalytic performance that is similar to pristine Fe Foam without amorphous domains. We also annealed the AB-treated R-Fe₂O₃ Foam (800 °C) in a vacuum at 1000 °C, and the highly efficient sample was transformed into a non-active catalyst. These control experiments strongly confirm that amorphous Fe domains in R-Fe₂O₃ Foam (800 °C) with abundant defects and vacancies are the active centers for the hydrolysis reaction. Supplementary Fig. 5d, h also shows the TEM images of R-Fe₂O₃ Foam (800 °C) after operation for 500 h, and the amorphous domains are well preserved, suggesting high stability in applications that require long device lifetimes.

Element B plays an important role in both reduction and hydrolysis processes where the amorphous domains with abundant defects and vacancies may react with B and form a Fe-B intermediate that facilitates the reaction. The reaction of Fe³⁺ with borohydride solution was actually used to form Fe-B composites in oxygen-free conditions. Density functional theory (DFT) calculations have been used to understand the effect of a Fe-B intermediate. In Fig. 4a four models were thus built up. Pure Fe (110) and pure FeB crystal with (111) facet

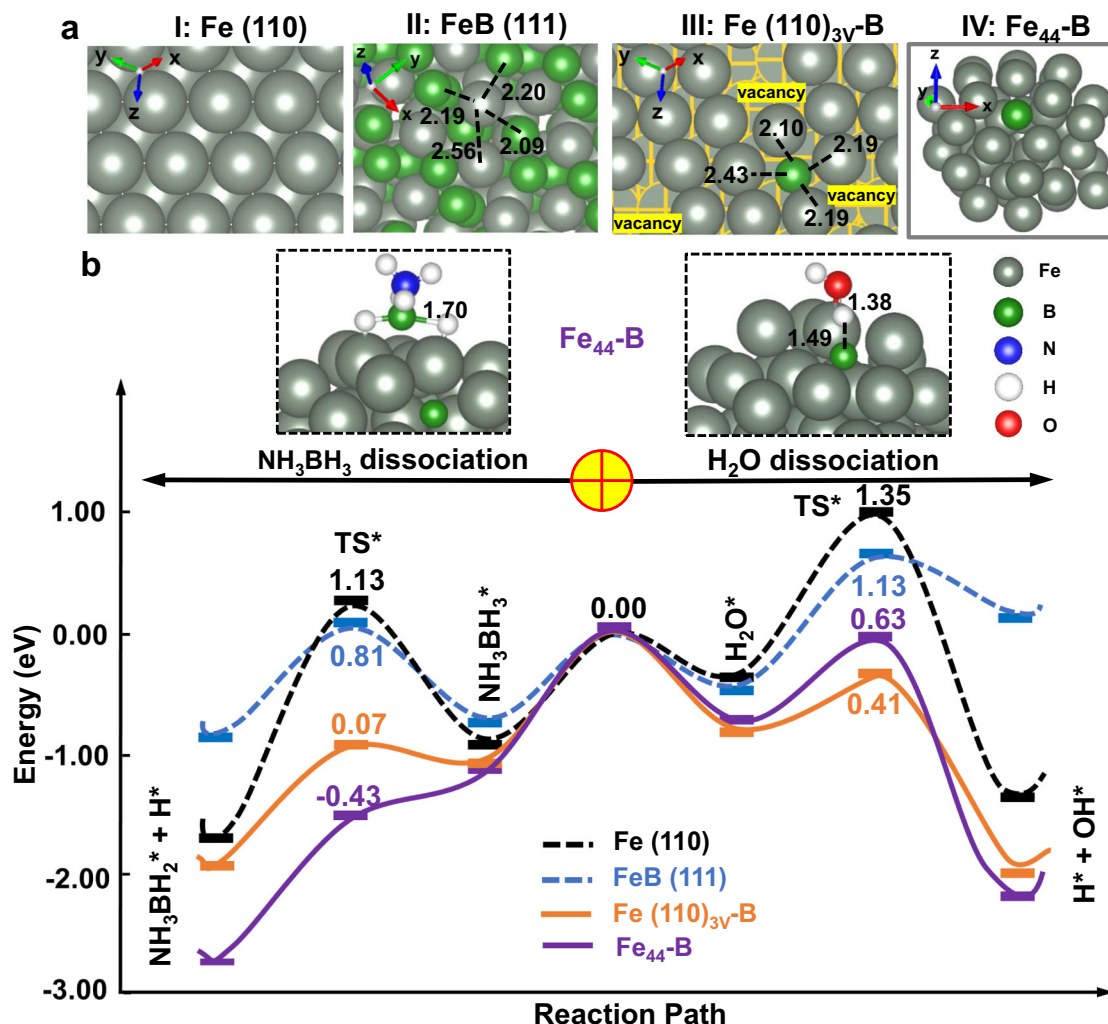


Fig. 4 | DFT calculations of the hydrolysis reaction. **a** 3D representations of four computational models: I: Fe (110), II: FeB (111), III: Fe (110)_{3V}-B, and IV: Fe₄₄-B. Color scheme: Fe (gray), B (green), O (red), N (blue), and H (white). **b** Energy profiles of NH₃BH₃ (left) and water (right) dissociated on the Fe (110), FeB (111), Fe (110)_{3V}-B, and Fe₄₄-B cluster surfaces. The top images show the transition states for AB and water dissociations on Fe₄₄-B, respectively. The reaction barriers of H₂O and AB

dissociations are calculated to be 0.63 eV (H₂O) and even no barrier (no TS*) with an energy decreasing of -0.43 eV (AB) on Fe₄₄-B, and are 0.41 eV (H₂O) and 0.07 eV (AB) on Fe (110)_{3V}-B, which are much lower than that on the other two reference models (pure Fe (110), 1.35 eV (H₂O) and 1.13 eV (AB); pure FeB (111), 1.13 eV (H₂O) and 0.81 eV (AB)).

(the dominant facet obtained in the experiment) were used as reference models. To simulate the Fe Foam with an amorphous region, both the Fe (110)_{3V}-B and Fe₄₄-B models were used. The Fe₄₄-B model was based on an amorphous Fe₄₄ cluster to simulate the amorphous Fe domain. It should be noted that there are too many possible surface models for the amorphous region, while in this work, we only select the representative Fe (110)_{3V}-B and Fe₄₄-B models for calculation. The Fe₄₄ cluster was first created by randomly removing 11 Fe atoms from a well-defined Fe₅₅ crystal cluster and then was optimized by structural relaxations to obtain the final amorphous Fe₄₄ cluster. A simulated XRD spectrum was performed to confirm its non-crystal characteristics. One B atom was located on a Fe vacancy to form the Fe₄₄-B model. To consider the effect of surrounded crystal Fe atoms along with the amorphous domain, the Fe (110)_{3V}-B model was also built up. Since the crystal face (110) was observed in TEM images, we have used Fe (110) as the base plane while the amorphous part was simulated by creating 3 Fe vacancies in the 16 atom unit (19 % vacancies), with a structure optimization along with the vacancies. One B atom was then located on a Fe vacancy to form the Fe (110)_{3V}-B model. In Supplementary Fig. 10, two additional models, Fe (110)_{3V} without B atom and Fe (110)_{1V} with B but fewer Fe vacancies (Fe (110)_{1V}-B), were also

compared. Adsorption energies of H₂O and AB on these six models are shown in Supplementary Fig. 10a. Both Fe (110)_{3V}-B and Fe₄₄-B exhibit moderate adsorption capability for H₂O and AB. Reaction pathways for the dissociation of H₂O and AB on Fe₄₄-B, Fe (110)_{3V}-B, Fe (110)_{1V}-B, Fe (110), and FeB (001) are presented in Supplementary Fig. 10b. Interestingly, the reaction barrier of H₂O dissociation on Fe₄₄-B is calculated to be a low value of 0.63 eV, and there is even no barrier with an energy decreasing of -0.43 eV for AB dissociation, in good agreement with the fast hydrolysis reaction based on R-Fe₂O₃ Foam (800 °C) (Fig. 4b). The reaction barriers of H₂O and AB dissociation on Fe (110)_{3V}-B are also low values of 0.41 and 0.07 eV, respectively (Fig. 4b). For comparison, the two barriers are considerably higher on pure Fe (110) (E_b = 1.35 (H₂O) and 1.13 (AB) eV, Fig. 4b) or pure FeB (111) (E_b = 1.13 (H₂O) and 0.81 (AB) eV, Fig. 4b). All the models with both Fe vacancy and B show low reaction barriers of H₂O and AB, while the pure amorphous model (Fe₄₄-B) has even no AB dissociation barrier when compared to the models with some vacancies and B. We further clarify the roles of vacancy and B. For the Fe (110)_{3V} model without B, the H₂O dissociation (0.66 eV) has been greatly enhanced when compared to pure Fe (110) (1.35 eV), suggesting the significant role of vacancies to enhance the performance. A similar Fe (110)_{1V} model with less vacancy

has also been calculated, showing an H₂O dissociation barrier (1.06 eV) between that of Fe (110)_{3V} and pure Fe (110). However, the AB dissociation on Fe (110)_{3V} without B is still high (0.53 eV) when compared to that of Fe (110)_{3V}-B (0.07 eV) or Fe₄₄-B (no energy barrier), suggesting a significant contribution from B. The Fe (110)-B model with B but without vacancies is also compared, with the high reaction barriers of H₂O (1.17 eV) and AB (0.84 eV) similar to that of pure Fe (110), confirming the key role of vacancies. Thus, the Fe-B intermediate in the amorphous region with large amounts of vacancies can significantly decrease the reaction barriers and improve the dissociation abilities of H₂O and AB, as proved by both the Fe₄₄-B and Fe (110)_{3V}-B models. Both Fe vacancy and B can contribute a lot to the catalytic performance. With these excellent dissociation properties, R-Fe₂O₃ Foam (800 °C) can significantly facilitate the formation of NH₃BH₂* and OH*, leading to the formation of NH₃BH₂OH intermediates that are favorable for the hydrolysis of AB^{6,27}. It should be noted that the first bond-breakings of O-H and B-H in H₂O and NH₃BH₃ are actually the rate-determining steps for the hydrolysis of AB^{28,29}, as shown in the full reaction cycle (see Methods part, DFT Calculations). Thus the R-Fe₂O₃ Foam (800 °C) shows an excellent catalytic performance. We also measured the hydrolysis performance of AB catalyzed by commercial FeB (Supplementary Fig. 11), which showed very low activity in good agreement with the calculations.

In situ XAS spectra at Fe K-edge are shown in Fig. 3c to probe the Fe-B interaction. The R-Fe₂O₃ Foam (800 °C) sample for the XANES measurements was quickly taken from the solution after working in AB solution for 7 h, which was fresh and fully reduced to avoid the influence of oxidation. The XANES spectrum of R-Fe₂O₃ Foam (800 °C) measured in air is similar to that of Fe Foam (see Fig. 2c). Interestingly, when immersed in AB solution to produce H₂, an increased feature A and a decreased feature B can be clearly observed, which can be attributed to the formation of Fe-B intermediate (similar to the spectrum of FeB)³⁰. For comparison, the pristine Fe Foam with fewer defects or vacancies (Supplementary Fig. 12a) shows only slight spectral changes when immersed in AB solution, suggesting weak or no formation of the Fe-B intermediate. The in situ spectral change of the R-Fe₂O₃ Foam (800 °C) sample strongly confirms the formation of the Fe-B intermediate during the reaction. In Supplementary Fig. 12b the EXAFS data of R-Fe₂O₃ Foam (800 °C) in AB also shows peak intensities higher than that in air, suggesting the coordination number increases with the Fe-B interaction²⁵. The fitting results in Supplementary Table 2 agree well with the formation of Fe-B intermediate. XANES spectrum of R-Fe₂O₃ Foam (800 °C) exposed to air again can be recovered, suggesting that the Fe-B intermediate mainly exists in the hydrolysis process. B K-edge XANES spectra have been used to further confirm the existence of Fe-B bonds in Fig. 3d. The main peak for all the samples can be attributed to B oxidized in air. However, a faint but clear Fe-B feature can be observed for R-Fe₂O₃ Foam (800 °C) (after immersion in AB), strongly supporting the existence of Fe-B. It should be noted that the B K-edge XANES spectra are more sensitive to the surface information (when compared to the Fe K-edge XANES spectra in the hard X-ray range), so the Fe-B residue in R-Fe₂O₃ Foam (800 °C) can be detected.

After the oxidation and reduction processes, amorphous domains can be created in the Fe Foam. The abundant defects and vacancies in amorphous domains can react with B to form Fe-B intermediate to decrease the reaction barriers and improve the dissociation abilities of H₂O and AB. The hydrolysis performance can thus be significantly enhanced. The amorphous domains in the samples treated at different temperatures are probed by TEM images in Supplementary Fig. 13, which are proportional to the catalytic activity (Supplementary Fig. 14). TEM image and elemental mappings of the spent catalyst are also shown in Supplementary Fig. 15. The amorphous domains in R-Fe₂O₃ Foam (800 °C) are also confirmed by the positron annihilation lifetime spectra (PALS) in Supplementary Fig. 16, in which the increased

lifetime (τ_2) with enhanced intensity (I_2) in R-Fe₂O₃ Foam (800 °C) strongly suggests the presence of large amounts of large size defects such as amorphous domains^{31,32}. Moreover, the Fe crystal structure acts as a solid framework for the active amorphous domains and maintains catalyst stability, leading to excellent long-term performance.

In summary, the facile, reproducible oxidation and reduction treatment of commercial Fe Foam demonstrated here has enabled the efficient and stable Fe catalysts for AB hydrolysis. The notable performances (TOF of 113.6 min⁻¹, about 771 L H₂ in 900 h, and 43.27 mL/(min·cm²) for 10 × 10 cm² of Foam) exceed reported benchmarks (most < 14 L H₂ in 45 h) and can even power a driven car in a commercial fuel cell (180 ml H₂/min, 7.5 wt% H₂, 7.8 V and 1.6 A for at least 5 h). Critically, the catalytic activity advantage offered by amorphous domains is combined with the stability brought by bulk crystal structures. These results are promising for the development of catalysts that can power vehicles by chemical storage in a hydrogen-based economy.

Methods

Materials preparation

Fe Foam was purchased with Fe purity higher than 98.2% (measured by an inductively coupled plasma (ICP) spectrometer). The Fe Foam is mainly metallic Fe, according to XRD data, while the surface has been oxidized in air. Except for the mentioned cases, Fe Foam with dimensions of 1 × 1 cm² and a thickness of 1.6 mm has been used in this work. The purchased Fe Foam has been carefully washed using acetone and ethanol with 15 min sonication. Then the Fe Foam was heated to 60 °C and kept for 5 h. For the oxidation process, the Fe Foam was sintered in a muffle furnace in air at 800 °C for 7 h and then naturally cooled for further reduction. The samples have been sintered at different temperatures (300, 500, and 1100 °C) for comparison. A similar method has been used to treat the Ni, Co, and Cu Foams (purchased with a purity higher than 98%).

For the reduction process, the oxidized Fe₂O₃ Foam was immersed in 3 M AB solution with 0.5 M NaOH for 20 min. Then the foam was thoroughly washed using water and ethanol for the hydrolysis of AB. The 20 min reduction in AB solution is good enough for excellent catalytic performance, though there is still some oxidized content in the R-Fe₂O₃ Foam. After a similar reduction process, R-NiO Foam (800 °C), R-CuO Foam (800 °C), and R-CoO Foam (800 °C) were also prepared. The catalytic performance is very stable even after working for 900 h. However, to exactly reveal the catalytic center, we used reduced foam after working in AB solution for 7 h for the XAS measurement, which can avoid the influence of the oxidized contents in the sample. Various reduction agents have also been used for comparison. The oxidized Fe₂O₃ Foam was also immersed in 3 M NaBH₄ or LiBH₄ solutions with 0.5 M NaOH for 20 min. For the N₂H₄ treatment, the oxidized Fe₂O₃ Foam was immersed in the solution containing 40 mL water and 20 mL N₂H₄ and then refluxed for 12 h at 95 °C. For the H₂ treatment, the oxidized Fe₂O₃ Foam was heated to 1100 °C (5 °C/min) in a furnace with the 10% H₂/Ar gas environment and then kept for 3 h.

Structural characterization

The samples were measured by a high-resolution transmission electron microscope (HRTEM) (FEI Talos F200x). The metal contents were measured by an inductively coupled plasma (ICP) spectrometer (VISTA-MPX (CCD Simultaneous ICP-OES), Varian). X-ray photoelectron spectrometer (XPS, Thermo Scientific K-Alpha+) and X-ray diffraction (XRD, PANalytical B.V. Empyrean powder diffractometer equipped with PIXcel3D detector) were used for the structure characterization. X-ray absorption spectroscopy (XAS) experiments were performed at the Shanghai Synchrotron Radiation Facility (SSRF, 11B) and the National Synchrotron

Radiation Laboratory (NSRL, Beamline MCD-B (Soochow Beamline for Energy Materials)). The in situ XAS experiments at Fe K-edge have been performed at beamline 11B at the SSRF. Positron annihilation lifetime spectra (PALS) are measured by using the BaF₂ detector with a high-resolution time of 210 ps. The radioactive isotope of ²²Na was used as the positron source with a total of 2 × 10⁶ counts. The PALS experiments are performed at the positron research platform of the Institute of High Energy Physics (IHEP) and analyzed with the program LT9.0.

Catalytic activity measurement

The R-Fe₂O₃ Foam (800 °C) was put in a one-neck round-bottom flask (25 mL) sealed, and connected to a gas collecting tube. Then 2 mL AB water solution (containing 3 mmol AB and 0.5 mmol NaOH, without NaOH the performance will slightly decrease but no significant influence) was quickly injected into the flask. The experiment was performed under room temperature and ambient atmosphere. The reaction time was recorded when observing the first bubble. The volume of hydrogen generation was measured by recording the displacement of water. A similar method was also used for the hydrolysis of LiBH₄ and NaBH₄ (2 mL water solution containing 3 mmol LiBH₄ or NaBH₄ with 0.5 mmol NaOH). The produced gas was identified as H₂ using a gas chromatograph (GC7890T system, using N₂ as carrier gas). The hydrolysis process can be described by the formula: NH₃BH₃ + 2H₂O = NH₄⁺ + BO₂⁻ + 3H₂. The area catalytic activity (A) is calculated by using the foam area: $A = V_{H_2} / (S_{Foam} \times t)$ in which V_{H₂} is the amount of produced H₂ (mL), S_{Foam} is the foam area (cm²), while t is the reaction time (min). For the long-term stability test, the R-Fe₂O₃ Foam (800 °C) (1 × 1 cm²) was put in a big flask with 413 mL AB solution containing 9.52 g AB. The hydrolysis was continuously catalyzed by R-Fe₂O₃ Foam (800 °C) for every 24 h (bubbles can be observed), and then the Foam was taken out to measure the catalytic activity in the 25 mL flask. The same Foam was put in the big flask again with fresh 413 mL AB solution to continue the stability test. It was measured for 900 h and the catalytic activity was measured several times (every 5 h in the first 100 h and every 100 h in the whole process). The TOF value has been calculated by using the surface layer Fe as the active site. The BET value of the R-Fe₂O₃ Foam (800 °C) is 2.3332 m²/g, while the weight of the Foam is 0.192 g. The diameter of the Fe atom is 0.28 nm, and the Fe Foam density is 7.874 × 10⁶ g/m³. Thus the amount of one surface layer Fe is $2.3332 \times 0.192 \times 0.28 \times 10^{-9} \times 7.874 \times 10^6 / 56 = 0.017$ mmol. The TOF value can be: $TOF = n_{H_2} / (n_{Fe(surface)} \times t) = 6 / (0.017 \times 3.106) = 113.6$ (H₂) mol/(Cat-Fe)mol·min.

DFT Calculations

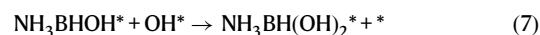
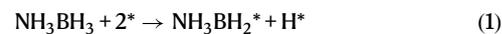
In the TEM image, the metallic Fe (110) in R-Fe₂O₃ Foam (800 °C) can be clearly observed. We thus chose the Fe (110) (cubic Fe (Im_{3m}) crystal) surface as the original plane for the following models: pure Fe (110), Fe (110)-B (with B but no vacancy), Fe (110)_{3V} (without B), Fe (110)_{1V}-B and Fe (110)_{3V}-B. The pure Fe (110) surface was simulated by 4 × 4 unit cells consisting of 4 atomic layers with 16 atoms per layer. To simulate the amorphous region, we created 3 Fe vacancies in the plane (3/16, around 19% vacancies) for Fe (110)_{3V}-B, and then optimized the atomic positions to form an amorphous state, as shown in Fig. 4a. For the Fe (110)_{1V}-B model, 1 Fe vacancy in the 4 × 4 unit cell (16 atoms) was used. Then one B atom was further introduced on the vacancy site according to the experimental observation from XAS. The Fe (110)_{3V} model without B was also constructed to reveal the B effect. It was worth noting that the B atom was more stable ($E_{binding} = -7.74$ eV) on the defect Fe (110) site than on the pure Fe (110) ($E_{binding} = -5.81$ eV) surface. Therefore, the present discussions are based on the more stable model with B located on a vacancy (Fe (110)_{1V}-B and Fe (110)_{3V}-B). In addition, we have also built the FeB (111) model ((111) is the dominant facet observed in the XRD spectrum of FeB) from the FeB crystal (Pnma) for comparison. A vacuum space of more than 15 Å was added

in the c-axis direction for all models to avoid interactions between the replicated cells.

To further approach the amorphous state, we have also created an amorphous Fe cluster to simulate the pure amorphous Fe domain. The amorphous Fe₄₄ cluster (containing 44 Fe atoms) was first created by randomly removing 11 Fe atoms from a well-defined Fe₅₅ crystal cluster. Then the created Fe₄₄ cluster was optimized by structural relaxations to obtain the final amorphous Fe₄₄ cluster. A simulated XRD spectrum of the Fe₄₄ cluster was performed to confirm its non-crystal characteristics. One B atom was located on a Fe vacancy to form the Fe₄₄-B model.

The geometry optimizations and energy calculations for all species were performed by means of periodic DFT with VASP 5.3 code³³. All atoms in the cell were permitted to relax during the following optimization processes. The generalized gradient approximation (GGA) with the Perdew-Burke-Ernzerh of (PBE) was applied to describe the exchange and correlation term³⁴, while the core-valence electron interactions were represented by using the project-augmented wave (PAW) method³⁵. The valence electrons for each atom were expanded in plane wave basis sets with cut-off energy at 400 eV. All intermediate states (IS) were optimized until the self-consistence reached 1·10⁻⁵ eV and 0.03 eV·Å⁻¹ for the electronic and the ionic convergence, respectively. The transition states (TS) related to the activation of water and NH₃BH₃ were obtained by combining the climbing-image nudged-elastic-band (CI-NEB) and improved-dimer (IDM) approaches^{36,37}. The TS was further confirmed by the existence of only one imaginary frequency along the reaction coordinate. The preliminary CI-NEB steps were converged to energies <1·10⁻⁴ eV and forces <0.1 eV·Å⁻¹ for electronic energies and geometries, respectively, while the convergence criteria for dimer steps were <1·10⁻⁷ and <0.05 eV·Å⁻¹. The reciprocal space in slab models was described by using a 3 × 3 × 1 k-point grid mesh, and Γ point was used for isolated H₂O and NH₃BH₃ molecules.

The full reaction cycle for DFT calculation could be described in the following steps^{28,29}:



Since the first bond-breakings of O-H and B-H in H₂O and NH₃BH₃ molecules was generally the rate-determining step during the whole

reaction cycle, we focused on the calculation and discussion of these two initial processes on the Fe-based catalysts.

Data availability

The data that support the plots in this article and other findings of this study are provided as a Source Data file. Source data are provided in this paper. Source data are provided in this paper.

References

- Chen, Z. et al. Balancing volumetric and gravimetric uptake in highly porous materials for clean energy. *Science* **368**, 297–303 (2020).
- Glenk, G. & Reichelstein, S. Economics of converting renewable power to hydrogen. *Nat. Energy* **4**, 216–222 (2019).
- Liu, S. et al. Hydrogen storage in incompletely etched multilayer Ti_2CT_x at room temperature. *Nat. Nanotech.* **16**, 331–336 (2021).
- DuanMu, J. W. & Gao, M. R. Advances in bio-inspired electrocatalysts for clean energy future. *Nano Res.* **17**, 515–533 (2024).
- Gao, F. Y. et al. Towards reliable assessment of hydrogen oxidation electrocatalysts for anion-exchange membrane fuel cells. *Nano Res.* **16**, 10787–10795 (2023).
- Peng, C. et al. Nanostructured Ni_2P as a robust catalyst for the hydrolytic dehydrogenation of ammonia-borane. *Angew. Chem. Int. Ed.* **54**, 15725–15729 (2015).
- Chandra, M. & Xu, Q. A high-performance hydrogen generation system: transition metal-catalyzed dissociation and hydrolysis of ammonia-borane. *J. Power Sources* **156**, 190–194 (2006).
- Li, P., Aijaz, A. & Xu, Q. Highly dispersed surfactant-free nickel nanoparticles and their remarkable catalytic activity in the hydrolysis of ammonia borane for hydrogen generation. *Angew. Chem. Int. Ed.* **51**, 6753–6756 (2012).
- Singh, S. K., Singh, A. K., Aranishi, K. & Xu, Q. Noble-metal-free bimetallic nanoparticle-catalyzed selective hydrogen generation from hydrous hydrazine for chemical hydrogen storage. *J. Am. Chem. Soc.* **133**, 19638–19641 (2011).
- Muir, S. S. & Yao, X. Progress in sodium borohydride as a hydrogen storage material: development of hydrolysis catalysts and reaction systems. *Int. J. Hydrogen Energy* **36**, 5983–5997 (2011).
- Dinc, M., Metin, Ö. & Özkar, S. Water soluble polymer stabilized iron(0) nanoclusters: A cost-effective and magnetically recoverable catalyst in hydrogen generation from the hydrolysis of sodium borohydride and ammonia borane. *Catal. Today* **183**, 10–16 (2012).
- Akbayrak, S., Tonbul, Y. & Özkar, S. Magnetically separable $\text{Rh}_0/\text{Co}_3\text{O}_4$ nanocatalyst provides over a million turnovers in hydrogen release from ammonia borane. *ACS Sustain. Chem. Eng.* **8**, 4216–4224 (2020).
- Yu, C. et al. Maximizing the catalytic activity of nanoparticles through monolayer assembly on nitrogen-doped graphene. *Angew. Chem. Int. Ed.* **57**, 451–455 (2018).
- Feng, K. et al. $\text{Cu}_x\text{Co}_{1-x}\text{O}$ nanoparticles on graphene oxide as a synergistic catalyst for high-efficiency hydrolysis of ammonia-borane. *Angew. Chem. Int. Ed.* **55**, 11950–11954 (2016).
- Hou, C. et al. Ternary Ni-Co-P nanoparticles as noble-metal-free catalysts to boost the hydrolytic dehydrogenation of ammonia-borane. *Energy Environ. Sci.* **10**, 1770–1776 (2017).
- Li, J. et al. Highly active and stable metal single-atom catalysts achieved by strong electronic metal-support interactions. *J. Am. Chem. Soc.* **141**, 14515–14519 (2019).
- Yan, H. et al. Bottom-up precise synthesis of stable platinum dimers on graphene. *Nat. Commun.* **8**, 1070 (2017).
- Demirci, U. B. & Miele, P. Hydrolysis of solid ammonia borane. *J. Power Sources* **195**, 4030–4035 (2010).
- US Department of Energy Office of Energy Efficiency and Renewable Energy and The FreedomCAR and Fuel Partnership. Targets for onboard hydrogen storage systems for light-duty vehicles https://www1.eere.energy.gov/hydrogenandfuelcells/storage/pdfs/targets_onboard_hydro_storage_explanation.pdf. (2009).
- Liu, L. et al. Making ultrastrong steel tough by grain-boundary delamination. *Science* **368**, 1347–1352 (2020).
- Smith, R. D. L. et al. Photochemical route for accessing amorphous metal oxide materials for water oxidation catalysis. *Science* **340**, 60–63 (2013).
- Anantharaj, S. & Noda, S. Amorphous catalysts and electrochemical water splitting: an untold story of harmony. *Small* **15**, 1905779 (2019).
- Li, Z. et al. A silver catalyst activated by stacking faults for the hydrogen evolution reaction. *Nat. Catal.* **2**, 1107–1114 (2019).
- Kang, J. et al. Amorphous domains in black titanium dioxide. *Adv. Mater.* **33**, 2100407 (2021).
- Xiao, Z. et al. Filling the oxygen vacancies in Co_3O_4 with phosphorus: an ultra-efficient electrocatalyst for overall water splitting. *Energy Environ. Sci.* **10**, 2563–2569 (2017).
- Demirci, U. B. Ammonia borane: an extensively studied, though not yet implemented, hydrogen carrier. *Energies* **13**, 3017 (2020).
- Xu, Q. & Chandra, M. A portable hydrogen generation system: catalytic hydrolysis of ammonia-borane. *J. Alloy. Compd.* **446–447**, 729–732 (2007).
- Zhang, H. H. et al. Refined alteration of active sites via O modification on $\text{CoP}/\text{Co}_2\text{P}@$ Carbon hetero-structural catalyst for hydrogen generation. *Appl. Catal. B-Environ.* **325**, 122324 (2023).
- Guan, Z. et al. Why do single-atom alloys catalysts outperform both single-atom catalysts and nanocatalysts on MXene? *Angew. Chem. Int. Ed.* **63**, e202316550 (2024).
- Puszkiew, J. A. Effect of Fe additive on the hydrogenation-dehydrogenation properties of $2\text{LiH} + \text{MgB}_2/2\text{LiBH}_4 + \text{MgH}_2$ system. *J. Power Sources* **284**, 606–616 (2015).
- Gao, R. et al. The role of oxygen vacancies in improving the performance of CoO as a bifunctional cathode catalyst for rechargeable Li-O₂ batteries. *J. Mater. Chem. A* **3**, 17598–17605 (2015).
- Jiang, X. et al. Characterization of oxygen vacancy associates within hydrogenated TiO_2 : A positron annihilation study. *J. Phys. Chem. C* **116**, 22619–22624 (2012).
- Perdew, J. P. et al. Atoms, molecules, solids, and surfaces: applications of the generalized gradient approximation for exchange and correlation. *Phys. Rev. B* **46**, 6671–6687 (1992).
- Blöchl, P. E. Projector augmented-wave method. *Phys. Rev.* **50**, 17953–17979 (1994).
- Henkelman, G., Uberuaga, B. P. & Jonsson, H. J. A climbing image nudged elastic band method for finding saddle points and minimum energy paths. *J. Chem. Phys.* **113**, 9901–9904 (2000).
- Henkelman, G. & Jonsson, H. J. A dimer method for finding saddle points on high dimensional potential surfaces using only first derivatives. *J. Chem. Phys.* **111**, 7010–7022 (1992).
- Monkhorst, H. J. & Pack, J. D. Special points for Brillouin-zone integrations. *Phys. Rev. B* **13**, 5188–5192 (1992).

Acknowledgements

We acknowledge the support from NSRL (MCD-B, Soochow Beamline for Energy Materials) and SSRF (11B) for the XAS experiments. This work is supported by the National Key R&D Program of China (2020YFA0406103 to J.Z.), the National Natural Science Foundation of China (51532001 to L.G., U1932211 to J.Z.), the Natural Science Foundation of Jiangsu Province (BK20220028 to Z.K.), Collaborative Innovation Center of Suzhou Nano Science & Technology, and the 111 Project.

Author contributions

J.Z., L.G., and J.L. designed the whole project. Y.C. performed most of the experiments. Z.L. contributed to DFT calculations. K.F. contributed to the XAS experiments. K.W. contributed to the demo. Y.L. and Z.K.

contributed to the experiments. All the authors discussed the results and contributed to writing the paper.

Competing interests

The authors declare no competing interests.

Additional information

Supplementary information The online version contains supplementary material available at <https://doi.org/10.1038/s41467-024-53574-x>.

Correspondence and requests for materials should be addressed to Lin Guo, Jun Zhong or Jun Lu.

Peer review information *Nature Communications* thanks Min-Rui Gao, Yong-Kul Lee, and the other anonymous reviewer(s) for their contribution to the peer review of this work. A peer review file is available.

Reprints and permissions information is available at <http://www.nature.com/reprints>

Publisher's note Springer Nature remains neutral with regard to jurisdictional claims in published maps and institutional affiliations.

Open Access This article is licensed under a Creative Commons Attribution-NonCommercial-NoDerivatives 4.0 International License, which permits any non-commercial use, sharing, distribution and reproduction in any medium or format, as long as you give appropriate credit to the original author(s) and the source, provide a link to the Creative Commons licence, and indicate if you modified the licensed material. You do not have permission under this licence to share adapted material derived from this article or parts of it. The images or other third party material in this article are included in the article's Creative Commons licence, unless indicated otherwise in a credit line to the material. If material is not included in the article's Creative Commons licence and your intended use is not permitted by statutory regulation or exceeds the permitted use, you will need to obtain permission directly from the copyright holder. To view a copy of this licence, visit <http://creativecommons.org/licenses/by-nc-nd/4.0/>.

© The Author(s) 2024